Journal of Oceanography, Vol. 56, pp. 567 to 581, 2000

Ocean Tide Models Developed by Assimilating TOPEX/POSEIDON Altimeter Data into Hydrodynamical Model: A Global Model and a Regional Model around Japan

KOJI MATSUMOTO[1]*, TAKASHI TAKANEZAWA[2] and MASATSUGU OOE[1]

[1]*Division of Earth Rotation, National Astronomical Observatory, Mizusawa 023-0861, Japan*
[2]*The Graduate University for Advanced Studies, Mizusawa 023-0861, Japan*

(Received 11 January 2000; in revised form 25 April 2000; accepted 17 May 2000)

A global ocean tide model (NAO.99b model) representing major 16 constituents with a spatial resolution of 0.5° has been estimated by assimilating about 5 years of TOPEX/POSEIDON altimeter data into barotropic hydrodynamical model. The new solution is characterized by reduced errors in shallow waters compared to the other two models recently developed; CSR4.0 model (improved version of Eanes and Bettadpur, 1994) and GOT99.2b model (Ray, 1999), which are demonstrated in comparison with tide gauge data and collinear residual reduction test. This property mainly benefits from fine-scale along-track tidal analysis of TOPEX/POSEIDON data. A high-resolution (1/12°) regional ocean tide model around Japan (NAO.99Jb model) by assimilating both TOPEX/POSEIDON data and 219 coastal tide gauge data is also developed. A comparison with 80 independent coastal tide gauge data shows the better performance of NAO.99Jb model in the coastal region compared with the other global models. Tidal dissipation around Japan has been investigated for M_2 and K_1 constituents by using NAO.99Jb model. The result suggests that the tidal energy is mainly dissipated by bottom friction in localized area in shallow seas; the M_2 ocean tidal energy is mainly dissipated in the Yellow Sea and the East China Sea at the mean rate of 155 GW, while the K_1 energy is mainly dissipated in the Sea of Okhotsk at the mean rate of 89 GW. TOPEX/POSEIDON data, however, detects broadly distributed surface manifestation of M_2 internal tide, which observationally suggests that the tidal energy is also dissipated by the energy conversion into baroclinic tide.

Keywords:
· Ocean tide,
· loading tide,
· satellite altimetry,
· assimilation,
· tidal energy dissipation.

1. Introduction

Since the launch of satellite altimeter TOPEX/POSEIDON (T/P), thanks to its unprecedented precise sea surface height data, the accuracy of ocean tide model has significantly improved especially in open ocean. The accuracy assessment by Andersen *et al*. (1995) suggested that the agreements of T/P-derived ocean tide models with open-ocean tide gauge data are better than those of the older Schwiderski (1980) and Cartwright and Ray (1991) models. Shum *et al*. (1997) indicated that the differences among eight T/P-based models are relatively small in deep ocean (ocean depth > 1000 m); for instance, the RMS differences for M_2 constituent is 0.97 cm. However, they pointed out that quite large differences occur mainly in shallow seas (ocean depth < 1000 m); the RMS differences is 9.78 cm for M_2. This result suggests that large ambiguities in recent ocean tide models still remain in shallow water region. We discuss the origins of errors in the tide models and aim at improving the ocean tide models in the shallow waters.

The modern global tide models can be categorized into three groups; (1) empirical model, (2) hydrodynamical model, and (3) assimilation model. All of the recent ocean tide models with each category have shortcomings as to the shallow water tide modelings.

The empirical model is based on only observational data, e.g., Eanes and Bettadpur (1994), Desai and Wahr (1995), and Ray (1999). Since the common data source of these models is T/P, the resulting resolution of models is limited by the ground track spacings of the satellite, and the model domain is also necessarily limited by the data coverage of the satellite (e.g., ±66° of latitude for T/P). The problem of coarse ground track spacings (2.83°

* Corresponding author. E-mail: matumoto@miz.nao.ac.jp

or 314 km at equatorial region for T/P) becomes critical in shallow waters where the ocean tides varies rapidly in space.

One can design the resolution of a hydrodynamical model as high as desired, depending upon the computer capacity. However, numerical hydrodynamical tide models always meet difficulties caused by the inaccuracies arising from inadequate bathymetric data and unknown frictional and viscosity parameters (Ray *et al.*, 1996) which especially affect the modeling of shallow water tides. Kantha (1995) also pointed out that it is difficult to obtain the tide model accurately in particular its phase model without extensive fine-tuning of control parameters such as the bottom friction. Although FES.94.1 model (Le Provost *et al.*, 1994) utilized finite element meshes and it has a very high resolution in shallow water regions, its accuracy in such regions is still questionable (see Subsection 5.2).

We believe that the assimilation method is the most promising one resolving the problem in shallow water regions. The problem of the empirical method with regard to the resolution can be compensated by the hydrodynamical model, and the inadequate potential of the hydrodynamical model can be recovered by observational data. Other advantages of the assimilation model over the empirical model are that (i) a truly global ocean tide model can be developed by extrapolating the model beyond the area of latitudes 66° (N or S) which is the limit of T/P ground tracks, and that (ii) erroneous altimetric tidal solutions contaminated by non-tidal ocean variability can be corrected for, in other words, the hydrodynamics is expected to act as an effective data filter. However, many investigators of assimilative models have not paid attention so far to the nature of shallow water tides, that is, the predominant short-wavelength components in shallow waters. Le Provost *et al.* (1995) corrected for the long-wavelength error only by altimetric tides in their previous FES.94.1 model. Egbert *et al.* (1994) and Matsumoto *et al.* (1995) constrained the hydrodynamic model by coarsely distributed crossover data. Kantha (1995) applied Desai and Wahr (1995) model to constrain only the deep region of his model.

Han *et al.* (2000) assimilated T/P-derived along-track M_2 solutions into three-dimensional hydrodynamical model off Newfoundland. They discussed about the advantage of an assimilation model for ocean tides in shallow water region. We basically follow this approach which is characterized by making the altimetric tidal estimation within small bins along the T/P ground tracks, in order to conserve the short-wavelength characteristics of shallow

Table 1. Summary of the tidal modeling schemes, in which EMP = empirical model; ASS = assimilation model; BGM = background model; AM = analysis method; RES = response method; HAR = harmonic method; FCN = FCN resonance effect is included in the response analysis or not; RAD = radiational potential is included in the response analysis or not; AS = assimilation scheme; REP = representer method of Egbert *et al.* (1994); NUD = nudging; OLI = optimal linear interpolation; AB = altimetric boundary condition; ATS = along-track tidal solutions; EE = estimation error of altimetric solution is taken into account in assimilation or not; SAL = self-attraction/loading effect is taken into account or not; SAL_LA = linear approximation of SAL; SAL_SCH = SAL computed from Schwiderski (1980) model; SAL_NAO.99b = SAL computed from NAO.99b model (this study).

Author	Type	BGM	AM	FCN	RAD	AS	AB	EE	SAL
Eanes and Bettadpur (1994) (CSR model)	EMP	FES.94.1	RES	No	No	—	—	—	—
Desai and Wahr (1995) (DW model)	EMP	—	RES	Yes	No	—	—	—	—
Ray (1999) (GOT99.2b model)	EMP	FES.94.1 and others	HAR	—	—	—	—	—	—
Le Provost *et al.* (1995) (FES.95.2 model)	ASS	FES.94.1	—	—	—	REP	CSR2.0	No	SAL_SCH
Kantha (1995)	ASS	—	—	—	—	NUD	DW	No	SAL_LA
Han *et al.* (2000)	ASS	—	RES	No	Yes	OLI	ATS	Yes	No
This study (NAO.99b model)	ASS	—	RES	Yes	Yes	NUD	ATS	Yes	SAL_NAO.99b

water tides. We counted in the free core nutation resonance effect and solar radiational effect for the better tidal analysis. The empirical tidal solution based on observation is used as an important constraint in the hydrodynamical model in which self-attraction/loading effect is precisely estimated. Here, the hydrodynamical model is used as an interpolation device to develop a merged ocean tide model. Table 1 summarizes modeling scheme of seven selected models including this study to make the methodology of this study more clear. We develop a global ocean tide model (NAO.99b model) and a regional ocean tide model around Japan (NAO.99Jb model) for 16 major constituents, i.e., M_2, S_2, N_2, K_2, $2N_2$, μ_2, ν_2, L_2, T_2, K_1, O_1, P_1, Q_1, M_1, OO_1, and J_1.

2. TOPEX/POSEIDON Data Processing

We processed about five years of the MGDRB (Merged Geophysical Data Records generation B) of the cycles 9-198. Our data processing procedure consists of the following five steps; (1) Unreliable data are eliminated by using the flag information contained in the MGDRB. The rejection criterion described in USER'S HANDBOOK Section 3.4 (Benada, 1997) was applied. However, we totally ignored ocean tide model flags (GEO_BAD_2 bits 1–4). (2) The 1 Hz MGDRB data are interpolated to geographically fixed normal points in order to prevent the geoid gradients from contaminating sea surface height. (3) The standard geophysical correction excluding ocean tidal correction is applied to sea surface height to form residual sea surface height ζ. (4) The dominant short-wavelength spatial variations of non-tidal signal are removed from ζ by an along-track low-pass filtering by using a Gaussian filter with e-folding scale of 1°. However, the application of the low-pass filtering is limited to deep seas (depth > 1000 m), because wavelength of ocean tide might be short in the order of 100 km or less in shallow waters. (5) The filtered (in deep seas) or unfiltered (in shallow seas) residual height is averaged over small bins which are gridded along the ground tracks. The grid sizes are 0.5° for global model and 1/12° for regional model, which are the same as the spatial resolution chosen for the hydrodynamical model. By cycle-by-cycle processing, we obtained the time series of residual sea surface height in each grid.

3. Tidal Analysis

The residual sea surface heights are analyzed within each grid using the response method (Munk and Cartwright, 1966). The notable feature of the response method is that the method does not insist upon expressing the tides as sums of harmonic functions of specified tidal spectral line, but expressing the tides by smooth admittance functions of each tidal species. Advantages of the response method over standard harmonic decomposition method in altimetric along-track tidal analysis is described by Ray (1998b). Observation equation using the response method with the orthotide extension by Groves and Reynolds (1975) is represented as

$$\zeta(t) = \sum_{m=0}^{2} \sum_{l=0}^{l_m} \left[U_{ml} P_{ml}(t) + V_{ml} Q_{ml}(t) \right] + C \qquad (1)$$

where $P_{ml}(t)$ and $Q_{ml}(t)$ are the orthotide functions which are formed by forcing equilibrium tides, U_{ml} and V_{ml} are the unknown parameters to be solved for, and C is also unknown parameter which represents the offset in ζ due to mean sea surface error, mean non-tidal sea surface dynamic topography, and geographically correlated orbit error. We set $l_0 = 0$ and $l_1 = l_2 = 2$. $l_0 = 0$ means that we assigned a constant admittance for the long period tides in which we included annual (S_a) and semi-annual (S_{sa}) tides.

The standard response-orthotide method is slightly modified to include the free core nutation (FCN) resonance effect and the radiational potential. Since the FCN eigenfrequency (about 1 + 1/430 cycle per sidereal day) is well within the diurnal tidal band, there will be a corresponding resonance in the Earth's response to the diurnal tidal force, and hence the forced nutations and body tide should be resonant at this frequency (Wahr and Sasao, 1981). The effect of the FCN on ocean tide can be taken into account by replacing the amplitudes of diurnal equilibrium tides with those multiplied by the following factor,

$$\overline{R}\left(\omega_{21j}\right) = \frac{1 + \tilde{k}_2\left(\omega_{21j}\right) - \tilde{h}_2\left(\omega_{21j}\right)}{1 + k_2 - h_2} \qquad (2)$$

where k_2 and h_2 are nominal Love numbers, $\tilde{k}_2$ and $\tilde{h}_2$ are frequency-dependent Love numbers of Wahr (1981) depending on FCN frequency for which 1 + 1/433.2 cycles per sidereal day (Herring *et al.*, 1986) is applied.

The solar radiation indirectly affects S_2 tide and its elliptical satellite T_2 tide through atmospheric tides. Cartwright and Ray (1994) suggested that this atmospheric loading effect can be taken into account by multiplying the amplitude of tide generating potential of S_2 and T_2 by 0.97 and lagging their phases by 5.9°. This adjustment is also applied to our analysis. We expect that cross-talk between S_2 and K_2 are reduced and K_2 constituent is improved (see Cartwright and Ray (1994) for details).

U_{ml}, V_{ml} and C are determined by the least squares method. Estimation errors e_m for each species m are simultaneously calculated in solving equation (1). They are then normalized by the averaged value of the estimation

errors over all the estimation grids ($\bar{e}_m = e_m/\sum e_m$), which are used to define the modification factor in Eq. (13) (see Subsection 4.3). The histogram of $\bar{e}_m$ (not shown) is bimodal. About 69% of the T/P grids have value of $\bar{e}_m$ = 1.0 ± 0.1, and 19% of them have value of $\bar{e}_m = 0.7 \pm 0.1$. The latter mainly consists of the grids in which cross-over points are contained, i.e., more data are available compared to the standard single-track grids. The amplitude and the Greenwich phase of 16 major constituents are directly calculated from U_{ml} and V_{ml}. These altimeter-derived tidal solutions are hereinafter referred to as T/P solutions.

4. Hydrodynamical Model and Assimilation

4.1 Hydrodynamical model

The hydrodynamical model used in this study is based on the tidal equations derived by Schwiderski (1980), which is a two-dimensional depth-integrated shallow water equations. We improved them by estimating secondary loading effect more precisely, and by adding advection term. It is appropriate to express the momentum equations and the continuity equation in spherical polar coordinate (R, λ, θ) = (Earth's mean radius (=6.371×10^6 m), east longitude, colatitude), because the curvature of the Earth can not be neglected for a global calculation of ocean tides. These equations are

$$\frac{\partial U}{\partial t} + A_\lambda = \frac{gH}{R\sin\theta}\frac{\partial}{\partial\lambda}\left(\tilde{\gamma}_2\eta + \xi - \zeta_o\right) - 2\Omega V\cos\theta + F_\lambda^b + F_\lambda^e \tag{3}$$

$$\frac{\partial V}{\partial t} + A_\theta = \frac{gH}{R}\frac{\partial}{\partial\theta}\left(\tilde{\gamma}_2\eta + \xi - \zeta_o\right) + 2\Omega U\cos\theta + F_\theta^b + F_\theta^e \tag{4}$$

$$\frac{\partial\zeta_o}{\partial t} = -\frac{1}{R\sin\theta}\left[\frac{\partial(V\sin\theta)}{\partial\theta} + \frac{\partial U}{\partial\lambda}\right] \tag{5}$$

where η, ξ and ζ_o are forcing equilibrium tide, self-attraction/loading (hereinafter referred to as SAL) term induced by ocean tide, and ocean tidal elevation to be modeled with respect to ocean bottom, respectively; g (=9.81 ms^{-2}) the gravity acceleration; Ω (=7.2722×10^{-5} radian s^{-1}) the Earth's angular velocity; H the local ocean depth which is taken from ETOPO5; $\tilde{\gamma}_2 = 1 + \tilde{k}_2 - \tilde{h}_2$; U and V the east and south velocities which are integrated from the surface to the bottom of the ocean. A_λ and A_θ are advection terms, which are retained only for the regional tide model around Japan, being expressed as

$$A_\lambda = \frac{1}{R}\frac{\partial(UV/H)}{\partial\theta} - \frac{UV\overline{H}_\theta}{HR} + \frac{1}{R\sin\theta}\left[\frac{\partial\left(U^2/H\right)}{\partial\lambda} - \frac{U^2\overline{H}_\lambda}{H}\right] + \frac{2UV\cot\theta}{HR} \tag{6}$$

$$A_\theta = \frac{1}{R}\frac{\partial\left(V^2/H\right)}{\partial\theta} - \frac{V^2\overline{H}_\theta}{HR} + \frac{1}{R\sin\theta}\left[\frac{\partial(UV/H)}{\partial\lambda} - \frac{UV\overline{H}_\lambda}{H}\right] + \frac{V^2 - U^2\cot\theta}{HR} \tag{7}$$

where

$$\overline{H}_\theta = \frac{1}{H}\frac{\partial H}{\partial\theta} \quad \text{and} \quad \overline{H}_\lambda = \frac{1}{H}\frac{\partial H}{\partial\lambda}.$$

The bottom friction terms (F_λ^b and F_θ^b) are written as

$$F_\lambda^b = -\frac{BU}{H^2}\left(U^2 + V^2\right)^{1/2} \tag{8}$$

$$F_\theta^b = -\frac{BV}{H^2}\left(U^2 + V^2\right)^{1/2} \tag{9}$$

where the bottom friction coefficient is defined as B = $0.0026 \times \mu\sin\theta$, μ being the grading parameter of Schwiderski (1980). The eddy viscosity terms (F_λ^e and F_θ^e) are also fully described by Schwiderski (1980).

In many numerical tidal models, the secondary SAL term ξ is approximated by linear relationship with local ocean tidal height as $\xi = \beta\zeta_o$, where values of 0.05 to 0.12 are empirically used for constant β. However, Matsumoto (1997) and Ray (1998a) pointed out that the scalar approximation yields large error near coast and there is no appropriate global constant generally chosen for β. It is required for accurate tidal modeling in particular to shallow waters that ξ be calculated by global integrals of the tidal elevation as (e.g., Hendershott, 1972)

$$\xi(\theta,\lambda) = \sum_{n=0}^{n_{\max}} \frac{3}{2n+1}\cdot\frac{\rho}{\bar{\rho}}\cdot\left(1 + k_n' - h_n'\right)\cdot\zeta_{o(n)}(\theta,\lambda) \tag{10}$$

where ρ (=1035 kg m^{-3}) and $\bar{\rho}$ (=5516 kg m^{-3}) are the mean density of sea water and the Earth, respectively; k_n' and h_n' are potential and deformational load Love numbers, respectively; $\zeta_{o(n)}$ is n-th degree spherical harmonic of tidal elevation as

$$\zeta_o(\theta,\lambda) = \sum_{n=0}^{n_{\max}} \zeta_{o(n)}(\theta,\lambda) \tag{11}$$

where we decomposed tidal elevation field up to degree $n_{\max} = 360$.

For numerical computations, discrete equations are developed corresponding to the continuous equations (3), (4), and (5), with 0.5° × 0.5° grid system for the global model and 1/12° × 1/12° grid system for the regional model around Japan. The latter has the model domain of (110°E–165°E, 20°N–65°N). We design a fully staggered finite-difference scheme following Schwiderski (1980). The computational northern limit for the global model was set at $\theta = 3°$ to avoid the singular point problem in the north pole. FES.95.2 model (Le Provost *et al.*, 1995) was used to provide boundary condition for the grids of $\theta \le 3°$. The mathematical boundary conditions adopted are no-flow across the ocean shorelines and free-slip along the ocean shorelines. The free-slip condition is more plausible in turbulent flows which have only thin boundary layers (Schwiderski, 1980). The no-slip condition was also tested, but the difference was very small. The discrete equations are numerically integrated with time, and time step is set to 93 sec for the global model and 15.5 sec for the regional model.

4.2 Tide gauge data

In order to gain accuracy in the coastal region, the regional model is assimilated with 219 coastal tide gauge data around Japan and Korea in addition to the T/P solutions. The data around Japan are provided by the Japan Oceanographic Data Center (JODC), and those around Korea are kindly provided by Dr. T. Yanagi. The original data set of JODC contains harmonic constants from 714 tide gauge stations, but the number of reported constituents are different by every station. The number of constituents is chosen as a quality index based on an assumption that the longer operated stations generally maintain more constituents and provide high quality data. We selected 155 gauges with more than 39 constituents as the most accurate internal gauges and assimilated into the hydrodynamical model. Apart from these gauges we selected 80 external gauges with more than 9 (and less than 40) constituents which is used for accuracy assessment (TG-C in Subsection 5.1). 64 gauges around Korea are chosen, but only for M_2, S_2, K_1, and O_1 constituents which are all used for assimilation. The geographical distribution of selected gauges around Japan are plotted in Fig. 1.

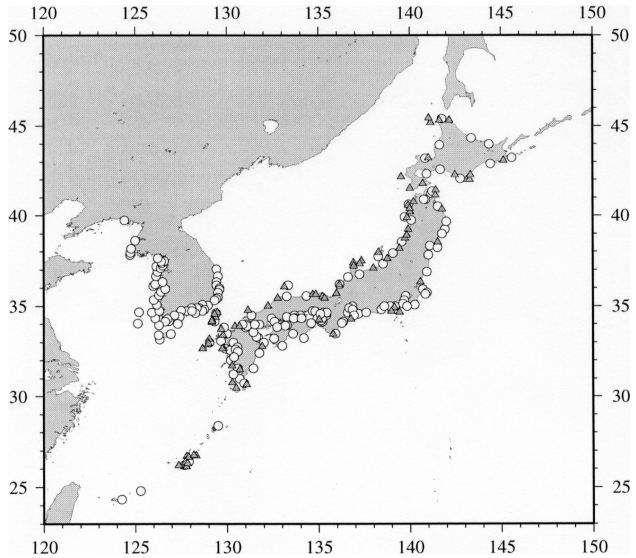

Fig. 1. Location of coastal tide gauge data around Japan used for regional assimilation (circles) and for accuracy assessment (triangles, TG-C in Subsection 5.1).

4.3 Assimilation

The T/P solutions and tide gauge data are incorporated into hydrodynamical model at this assimilation stage. We employ a rather simple assimilation procedure so-called blending method. This method was also introduced in tidal modeling and its efficiency was presented in Kantha (1995) and Matsumoto *et al.* (1995). The model-predicted tidal height ζ_{MODEL} at time step (i) is replaced by a weighted sum of the model prediction and the observed T/P tidal height.

$$\zeta_o' = f_{mj} \cdot \zeta_{\mathrm{T/P}} + \left(1 - f_{mj}\right) \cdot \zeta_{\mathrm{MODEL}} \tag{12}$$

$$f_{mj} = \frac{f^c_{mj}}{\bar{e}_m} \tag{13}$$

where ζ_o' is modified tidal height to be used to calculate the velocities U and V at next time step ($i + 1$), $\zeta_{\mathrm{T/P}}$ is the tidal hight predicted by the T/P solution with the normalized formal error of $\bar{e}_m$.

The constant values $f^c{}_{mj}$ were determined after some trial-and-error computations so that the tidal solutions obtained become smooth in space to some extent. The employed values of $f^c{}_{mj}$ are 0.5 for M_2, 0.4 for S_2, 0.25 for N_2, K_2, K_1, O_1, and P_1, 0.1 for Q_1, 0.05 for $2N_2$, μ_2, ν_2, L_2, and T_2, 0.02 for M_1, OO_1, and J_1. A similar method is also applied to the tide gauge data in regional tide modeling, but we assigned a constant nudging factor of $f_{mj} = 0.95$ to the tide gauge data, because published tidal constants from tide gauges are not usually accompanied with their estimation error.

Before stepping forward to final solutions, the fol-

lowing iterative process is necessary as for SAL tide. (1) It is necessary to know spatial distribution of ocean tidal height ζ_o to calculate the SAL tides which is suggested from Eq. (10). The initial tidal field were calculated with the linear approximation $\xi = 0.1\zeta_o$ as the first-guess result from which SAL tides were then estimated. (2) We reprocessed the MGDRB by replacing CSR3.0 radial loading values with those predicted by newly estimated radial loading charts associated with h_n' in Eq. (10). T/P solutions are also re-estimated from the reprocessed MGDRB data. (3) The linear approximation were replaced in the hydrodynamical model by more precise expression of Eq. (10) (SAL_NAO.99b) in the final calculation. The loading tide map is also re-estimated from the final ocean tidal solution.

First, we derived global model for major 16 constituents, then they were used to provide open boundary condition for regional tidal modeling around Japan. We separately ran the model for each constituent. Ten-cycle computation without assimilation was carried out as spin-up run and assimilation run was also carried out for ten-cycle period which was sufficient to obtain stable results. The amplitude and Greenwich phase values as model output were calculated by Fourier transform of tidal height from the last one cycle of computation.

5. Comparing Models

5.1 Internal comparison

In order to identify effective aspect of the present modeling approach in improving the results, we designed seven case runs for the global model and three case runs for the regional model. At first, bin size of global tidal analysis is changed to 2 degrees and 1 degree (cases 1 and 2) keeping the grid size of numerical model unchanged. Case 3 applies constant nudging factor (f_{mj} = f^{c}_{mj}). Cases 4 and 5 exclude FCN resonance effect and radiational effect out of the tidal analysis, respectively. Case 6 uses linear approximation of SAL tide (SAL_LA), for which β is set to Kantha's (1995) value of 0.054. Case 7 is the standard global model NAO.99b. Case 8 is a regional model which uses the SAL_LA and does not assimilate tide gauge data. Case 9 is a regional model which does not assimilate tide gauge data, and case 10 is the standard regional model NAO.99Jb. These case settings are summarized in Table 2.

The RMS misfits to three sets of tide gauge data are calculated for each case run about major eight constituents. The first set of the gauges is a globally distributed island and sea-bottom tide gauges in open ocean (98 stations) which were selected from the data compiled by C. Le Provost and other members (unpublished data). The second is shallow water (depth < 1000 m) pelagic tide gauges (58 stations) which were selected from Smithson (1992), and the third is the coastal tide gauge data around Japan (80 stations) provided by JODC (see Subsection

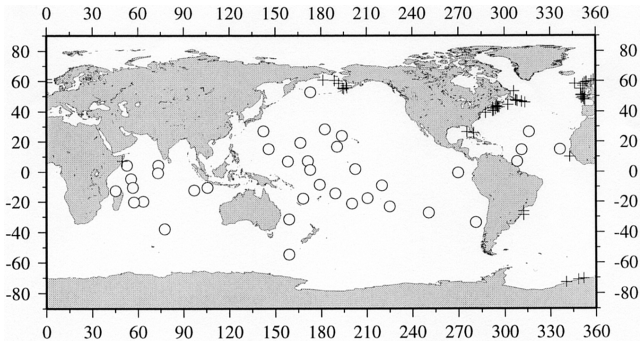

Fig. 2. Location of 98 island and sea-bottom tide gauge stations in the open ocean (circles, TG-A), and 58 shallow-water (depth < 1000 m) pelagic tide gauge stations (crosses, TG-B).

Table 2. Summary of case settings, in which BS = bin size in degrees used in the altimetric tidal analysis; NF = nudging factor; ED = error dependent; TG = coastal tide gauges around Japan are assimilated or not. See Table 1 for the description of FCN, RAD, SAL, SAL_NAO.99b, and SAL_LA.

Case	Domain	BS	NF	FCN	RAD	SAL	TG
1	Global	2.0	ED	Yes	Yes	SAL_NAO.99b	—
2	Global	1.0	ED	Yes	Yes	SAL_NAO.99b	—
3	Global	0.5	Constant	Yes	Yes	SAL_NAO.99b	—
4	Global	0.5	ED	No	Yes	SAL_NAO.99b	—
5	Global	0.5	ED	Yes	No	SAL_NAO.99b	—
6	Global	0.5	ED	Yes	Yes	SAL_LA	—
7	Global	0.5	ED	Yes	Yes	SAL_NAO.99b	—
8	Regional	1/12	ED	Yes	Yes	SAL_LA	No
9	Regional	1/12	ED	Yes	Yes	SAL_NAO.99b	No
10	Regional	1/12	ED	Yes	Yes	SAL_NAO.99b	Yes

4.2). We hereinafter refer to these three sets of tide gauges as TG-A, TG-B, and TG-C, respectively. The location of the tide gauge stations are plotted in Fig. 2 for TG-A and TG-B, and in Fig. 1 for TG-C (triangles). The RMS misfit is defined as

$$\mathrm{RMS} = \left[\frac{1}{N} \sum_{N} \frac{1}{2} \left(A_M^2 - 2A_M A_T \cos(\delta_M - \delta_T) + A_T^2 \right) \right]^{1/2} \quad (14)$$

where N is the number of stations, A and δ are amplitude and Greenwich phase with subscript M and T denoting the harmonic constants from ocean tide model and tide gauge data, respectively.

Figures 3, 4, and 5 show the results of the comparison with TG-A, TG-B, and TG-C, respectively, from which we introduce the following six remarks: (1) The smaller size of the T/P solution bin results in better accuracy. This has the largest impact on the accuracy improve-

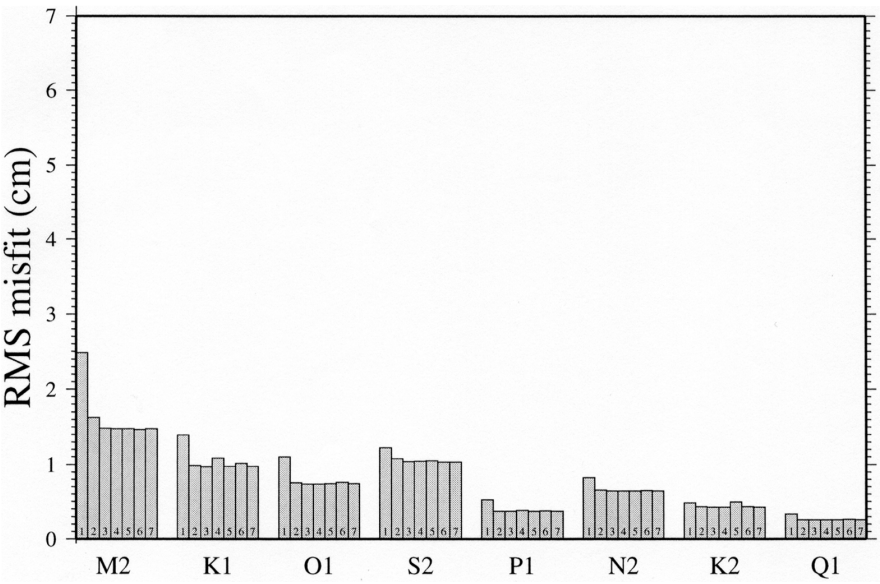

Fig. 3. RMS misfits to 98 open-ocean tide gauges (TG-A) which compare the accuracy of 7 case runs for the global model. The index of each case run is printed at the bottom of the bar. See Table 2 for the description of the case settings.

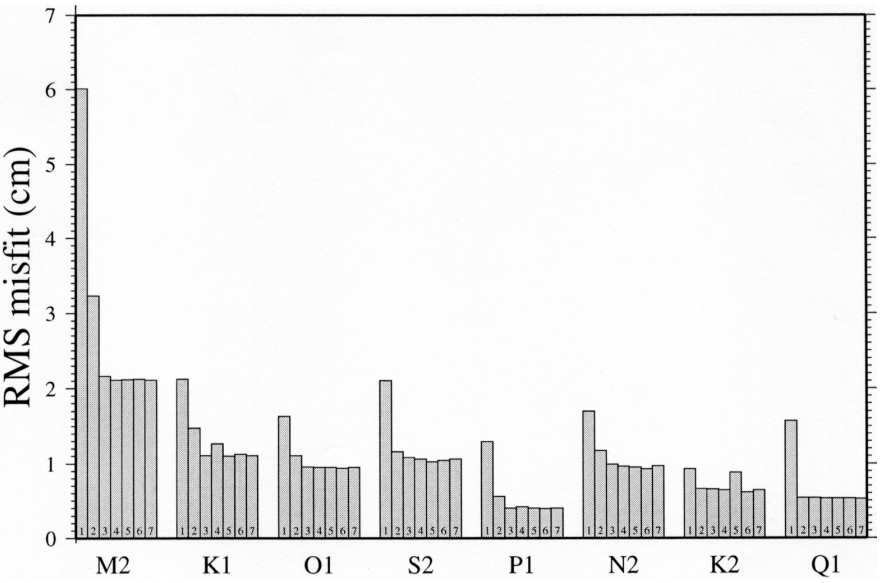

Fig. 4. Same as Fig. 3, but for 58 shallow-water tide gauges (TG-B).

ment of the global model. The relatively larger RMS errors of case 1 or 2 for shallow-water gauges (TG-B) than for open-ocean gauges (TG-A) suggest the lower performance of 1- or 2-degree grid to capture the short-wavelength feature of ocean tide in shallow seas. (2) The error-dependent nudging factor almost does not change RMS misfits. This is because the estimation errors of T/P solutions are generally larger in some specific seas which are covered by ice in winter, e.g., the Sea of Okhotsk, the Hudson Bay, and around the Antarctica. Advantage of the error-dependent nudging factor over the constant nudging factor is not clear in the present comparison in which few tide gauges are located at ice-covered seas. (3) K_1 and P_1 constituents are slightly (of the order of 1 mm) improved by including the FCN resonance effect as expected from the fact that their frequencies are relatively close to that of the FCN. This is shown by the smaller RMS error of case 7 than that of case 4. (4) The K_2 con-

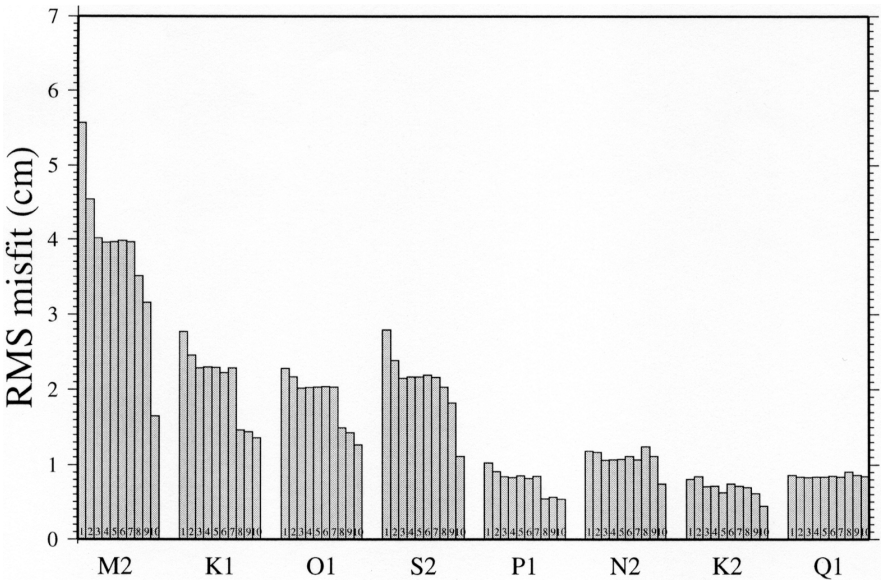

Fig. 5. Same as Fig. 3, but for 80 coastal tide gauges around Japan (TG-C). Also shown are additional comparisons of 3 case runs for the regional model (cases 8, 9, and 10).

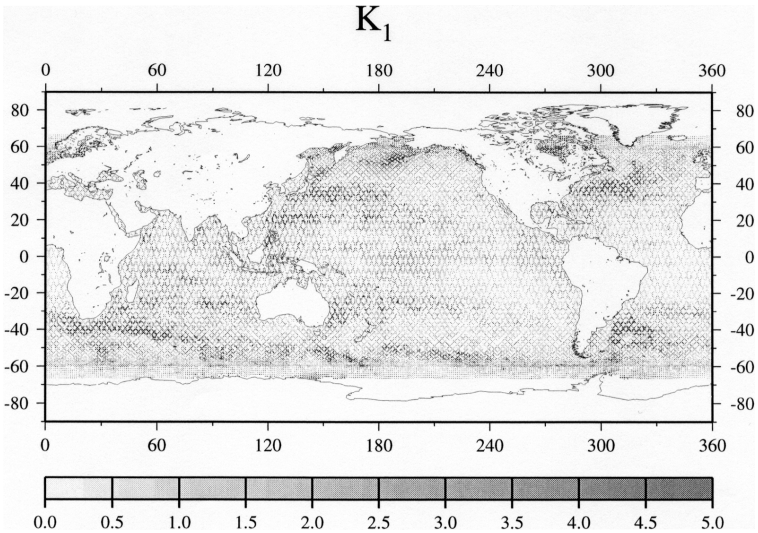

Fig. 6. Vector differences between T/P altimetric tidal solutions and the final assimilated solutions for K_1 constituent. Unit is in cm.

stituent is slightly improved by the fine structure of the admittance which includes radiational anomaly (compare cases 5 and 7). This is not the case for TG-C, but TG-A and TG-B give the RMS reduction of 0.7 mm and 2.4 mm, respectively. (5) For the global model, differences between results using SAL_LA (case 6) and SAL_NAO.99b (case 7) is marginal. However, the use of SAL_NAO.99b has a more evident effect on the regional model (compare cases 8 and 9). This is because the ratio of the number of T/P-constrained grid to that of total ocean grid is higher for the global model than for the regional model. In other words, if the grid size of a numerical model becomes smaller the altimetric constraint of the same size becomes sparser. And then the quality of the numerical model, which interpolates tides to the unconstrained region, becomes more important. (6) The coastal tide gauge data significantly improve the regional model (compare cases 9 and 10). Especially, M_2 RMS error reduction of 1.5 cm is realized by assimilating the coastal tide gauge data.

For the global model we made internal comparison between T/P solutions and final NAO.99b solutions. Figure 6 shows the geographical distribution of the vector differences between two solutions for K_1 constituent. Large differences are observed in strong current zones, such as the Kuroshio, the Gulf Stream, the Agulhas Current, or the Antarctic Circumpolar Current. They are also evident in the seas which are covered by ice in winter where less data are available. This means that the erroneous T/P solutions are effectively corrected for through the assimilation procedure. The discrepancies are largest for K_1 constituent for which global RMS of the vector differences is 2.31 cm, while those for M_2, O_1, and S_2 are 1.86 cm, 1.27 cm, and 1.27 cm, respectively. This suggests that the estimated admittance at K_1 frequency is affected, to a greater degree, by oceanographic variability. This is due to the fact that the aliasing period of K_1 tide (173.2 days) lies in near the period of Ssa which is primarily weather-driven and has typically wide spectral width.

5.2 Comparison with other models

We compared the NAO.99b model with the other two recent ocean tide models. One is CSR4.0 model (improved version of Eanes and Bettadpur, 1994) and the other is GOT99.2b model (Ray, 1999). The vector differences for M_2 between NAO.99b model and CSR4.0 model is shown in Fig. 7. The differences between NAO.99b model and GOT99.2b model (not shown) has similar spatial patterns. It means that the differences are smaller than 1 cm almost everywhere in the open ocean, but they are larger than 5 cm at some specific shallow seas; e.g., the Bering Sea, the Sea of Okhotsk, the Yellow Sea, the European shelf, the seas around Indonesia, the seas around Tasmania, the Amazon shelf, and Patagonian shelf. They are also seen in the regions polewards of the T/P limit of 66° where models are necessarily less accurate than elsewhere on the globe.

We employed two kinds of test in order to examine the accuracy of the ocean tide models. The first test is comparison with tide gauge data, and the second is a collinear residual reduction test. The results of the first test are summarized in Tables 3, 4 and 5 for TG-A, TG-B, and TG-C. The RMS values listed in Table 3 (TG-A) are comparable for all the models, as is expected from the fact that the model differences in the open ocean are

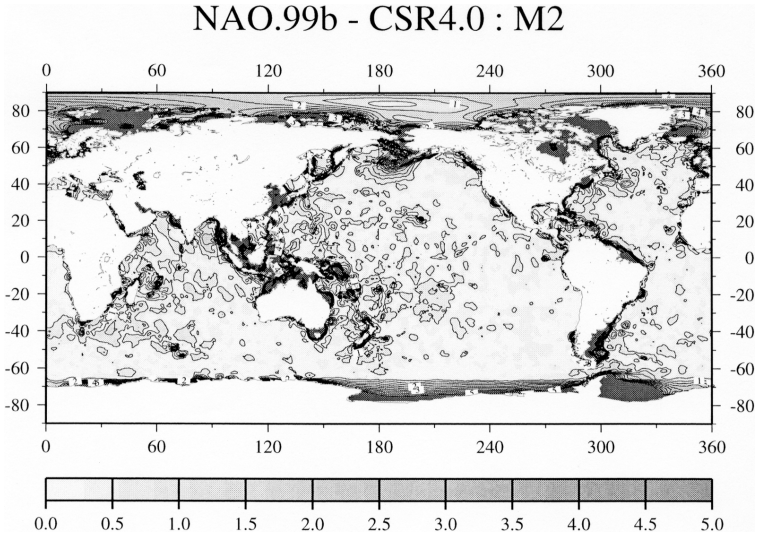

Fig. 7. Vector differences between NAO.99b model and CSR4.0 model (improved version of Eanes and Bettadpur, 1994). Contours are drawn up to 5 cm with interval of 0.5 cm.

Table 3. RMS misfits to open-ocean tide gauge data (TG-A). Unit is in cm. RSS is the root sum squares of major eight constituents.

Model	Wave													
	M_2	K_1	O_1	S_2	P_1	N_2	K_2	Q_1	RSS	$2N_2$	μ_2	ν_2	L_2	T_2
NAO.99b	1.457	1.011	0.755	1.033	0.378	0.643	0.426	0.261	2.364	0.253	0.418	0.201	0.403	0.296
CSR4.0	1.477	1.100	0.848	1.000	0.397	0.631	0.509	0.324	2.456	0.284	0.438	0.192	0.405	0.296
GOT99.2b	1.392	1.035	0.829	1.006	0.372	0.637	0.414	0.289	2.347	—	—	—	—	—
Number of stations	98	98	98	98	95	96	95	93		33	36	32	36	26

Table 4. RMS misfits to shallow water tide gauge data (TG-B). Unit is in cm. RSS is the root sum squares of major eight constituents.

Model	Wave								
	M_2	K_1	O_1	S_2	P_1	N_2	K_2	Q_1	RSS
NAO.99b	2.144	1.108	0.951	1.061	0.400	0.966	0.641	0.527	3.083
CSR4.0	4.477	1.191	1.309	1.245	0.433	1.094	0.844	0.523	5.205
GOT99.2b	2.451	1.138	1.305	1.023	0.382	0.742	0.657	0.491	3.379
Number of stations	58	58	58	58	58	58	58	58	

Table 5. RMS misfits to coastal tide gauge data around Japan (TG-C). Unit is in cm. RSS is the root sum squares of major eight constituents.

Model	Wave											
	M_2	K_1	O_1	S_2	P_1	N_2	K_2	Q_1	RSS	μ_2	ν_2	L_2
NAO.99Jb	1.648	1.360	1.268	1.112	0.535	0.740	0.445	0.838	3.024	0.964	0.219	0.538
NAO.99b	3.968	2.287	2.035	2.164	0.847	1.068	0.711	0.832	5.732	1.089	0.275	0.546
CSR4.0	4.911	2.344	2.259	2.653	0.776	1.322	0.729	0.864	6.737	1.104	0.253	0.574
GOT99.2b	4.173	2.366	2.260	2.274	0.791	1.098	0.793	0.847	6.038	—	—	—
Number of stations	80	80	80	80	80	80	80	80		78	78	77

relatively small. NAO.99b model shows the best agreement with TG-B among the three models. GOT99.2b model also performs well with TG-B. This seems because GOT99.2b uses, as a background model, the local ocean tide model of Lambert *et al.* (1998) in the Gulf of Maine and the Gulf of St. Lawrence instead of FES.94.1, while CSR4.0 model does not. The accuracy of an empirical model which solves for correction term to a background model depends on the quality of the background model in shallow waters. The comparison with the coastal tide gauge data (TG-C) shows the significant improvement of NAO.99Jb model over the other three global models. The RSS value for main eight constituents is the smallest with NAO.99Jb model (3.024 cm). The possible reasons for the larger RMS values as to TG-C than TG-A are that (1) model ambiguities are still larger in coastal region, and (2) the model resolution of 1/12° is still coarse for such local comparison. The reason (2) become critical if the tide gauges are subjected to local effects due to the shape of the bay and do not fully represent the tidal field around the stations.

The second test compares the model performances in terms of the degree of residual reduction at satellite measurement normal points. This test is based on the assumption that subtracting tides using a better tide model should result in a lower residual variance. The test is carried out over the T/P cycles 240–258, of which all the models compared are independent. The tide prediction software provided by each author is used to output elastic ocean tidal height (ocean tide + radial loading tide).

Table 6. RMS collinear residuals. Unit is in cm. *H* denotes the ocean depth. RMS values are calculated from T/P cycles of 240 to 258.

Model	Area			Total
	$H < 200$ m area 1	200 m $\le H <$ 1000 m area 2	$H \ge 1000$ m area 3	
NAO.99b	11.20	6.98	8.56	8.65
CSR4.0	15.77	7.37	8.55	8.96
GOT99.2b	13.99	7.37	8.65	8.92
Number of normal points	25609	18796	525054	569459

For NAO.99b model, besides the major 16 constituents additional minor 33 constituents are inferred from major ones by interpolating or extrapolating tidal admittance in frequency domain using second order polynomials.

In order to clarify the depth-dependence of residuals, we calculate RMS collinear residual within three regions of the ocean; the very shallow water region (H < 200 m, area 1), the shallow water region (200 m ≤ H < 1000 m, area 2), and the deep water region (H ≥ 1000 m, area 3). The RMS values are listed in Table 6 which shows the improvement of NAO.99b model in the shallow waters. NAO.99b model provides the smallest RMS values in area 1 of 11.20 cm compared with 15.77 cm for CSR4.0 model and 13.99 cm for GOT99.2b model. In area 2, NAO.99b model gives slightly smaller RMS value of 6.98 cm than CSR4.0 and GOT99.2b models (7.37 cm). The accuracy in the deep seas are comparable for all the models. However, Table 6 suggests that tidal prediction in continental shelf region (H < 200 m) still has larger ambiguity (11.20 cm) compared with that in deep seas (8.56 cm). The subtidal variability and non-linear tides which were omitted in both tidal analysis and the hydrodynamical model may be the main reason of this large RMS value.

6. Tidal Energetics around Japan

Although the accuracy of ocean tide models in terms of tidal elevation is significantly improved due to T/P precision altimetry, the issues of tidal energetics still remain unsolved. The total global rate of energy dissipation for M_2 constituent is now well established to be 2.5 ± 0.1 TW (1 TW = 10^{12} W). This value is deduced from three different space-geodetic technologies; lunar laser ranging (Dickey *et al.*, 1994), earth-orbiting satellite tracking (Christodoulidis *et al.*, 1988), and satellite altimetry (Cartwright and Ray, 1991). Although the global dissipation rate is precisely determined, how and where the energy is dissipated remains uncertain. The plausible candidates of the dissipater are friction in shallow seas and conversion of barotropic tidal energy to baroclinic one. The latter occurs mainly in ridge and island chain system, and estimates of baroclinic dissipation differ from author by author: for instance, Morozov's (1995) estimate of global M_2 baroclinic dissipation rate is 1.1 TW, but Kantha and Tierney (1997) estimated it as 360 GW (1 GW = 10^9 W). On the other hand, the dissipation by friction is generally dominant in shallow seas where tidal currents are stronger than in deep seas as described by Le Provost and Lyard (1997) who assumed the bottom friction as the only dissipation mechanism. Such regions include the Yellow Sea and the Sea of Okhotsk. Our focus here is on showing a preliminary result on the barotropic tidal energetics around Japan for dominant M_2 and K_1 constituents by using high-resolution NAO.99Jb model which is considered to reproduce more realistic tidal current than the global model NAO.99b.

Tidal energy flux vector $\boldsymbol{E}$ is expressed (Pugh, 1987) as

$$\boldsymbol{E} = \frac{1}{2}\rho g H A_\zeta \boldsymbol{A}_{uv} \cos\left(\delta_\zeta - \delta_{uv}\right) \qquad (15)$$

where (A_ζ, δ_ζ) are the amplitude and the phase of tidal elevation and ($\boldsymbol{A}_{uv}$, δ_{uv}) are the amplitude and the phase of depth-mean tidal currents of (u, v) = (U/H, V/H) components. The tidal energy fluxes are shown in Figs. 8 and 9 for M_2 and K_1, respectively.

The characteristic of M_2 tidal energy flux around Japan shows that the energy is mainly transferred to the south-west direction in the Pacific, and in particular, part of it enters into the Sea of Okhotsk and the East China Sea where it must be dissipated because of almost no flux goes out of the seas. The flux pattern of K_1 in the Pacific offshore is similar to that of M_2, but few flux enters onto the East China Sea and the most of energy seems to be dissipated in the Sea of Okhotsk. There is an energy flux gyre near to the place (155°E, 47°N) which is probably trapped by bottom topography. The topography-coherent flux is more evident along 1000 m isobath from (151°E,

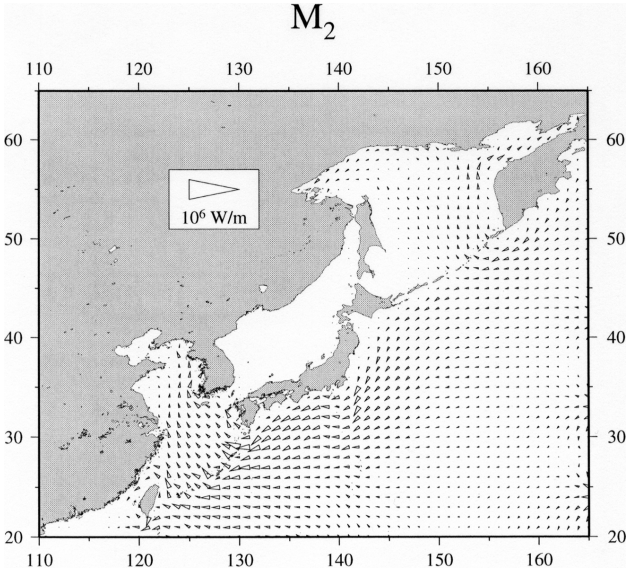

Fig. 8. M_2 ocean tidal energy flux vectors in Wm^{-1} of cross-section.

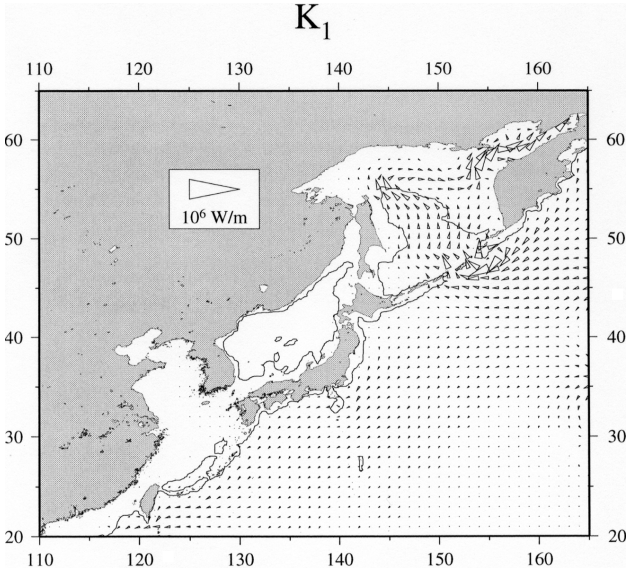

Fig. 9. Same as Fig. 8, but for K_1 energy flux. Superimposed is 1000 m isobath.

Table 7. Mean rate of tidal energy dissipation. Unit is in GW. D^b is the dissipation rate by bottom friction, D^e is the dissipation rate by eddy viscosity, and D is the sum of D^b and D^e.

Region	Mean dissipation rate					
	M_2			K_1		
	D^b	D^e	D	D^b	D^e	D
NAO.99Jb model domain (110°E–165°E, 20°N–65°N)	216	64	280	63	54	117
Region A (115°E–130°E, 20°N–45°N)	146	9	155	4	2	6
Region B (135°E–165°E, 45°N–65°N)	46	8	54	57	32	89

53°N) to (145°E, 55°N) where the flux turns its direction to the eastward forming V shape of the flux.

The mean rate of energy dissipation due to bottom friction D^b and eddy viscosity D^e is computed from the expression

$$D^b = -\frac{1}{T}\int_0^T \left(\iint_S \rho \boldsymbol{F}^b \cdot \boldsymbol{u} ds\right) dt \qquad (16)$$

$$D^e = -\frac{1}{T}\int_0^T \left(\iint_S \rho \boldsymbol{F}^e \cdot \boldsymbol{u} ds\right) dt \qquad (17)$$

where $\boldsymbol{F}^b = (F^b{}_\lambda, F^b{}_\theta)$ is the dissipation vector by bottom friction, $\boldsymbol{F}^e = (F^e{}_\lambda, F^e{}_\theta)$ is that by eddy viscosity, $\boldsymbol{u} = (u, v)$, and T is tidal period. The integration of total dissipation rate $D = D^b + D^e$ over the NAO.99Jb model domain gives 280 GW for M_2 and 117 GW for K_1, respectively. The main places where strong dissipation occurs are the East China Sea and the Yellow Sea region (region A; 115°E–130°E, 20°N–45°N), and the Sea of Okhotsk region (region B; 135°E–165°E, 45°N–65°N). Listed in Table 7 are the dissipation rates integrated over the three regions of NAO.99Jb model domain, region A, and region B.

As is expected from Fig. 8, high M_2 dissipation rates are calculated for the regions A and B where the integrated values are 155 GW and 54 GW, respectively, mostly accounted for by the bottom friction. These values are compared with estimates by Le Provost and Lyard (1997) of 182 GW and 73 GW which are lager than our estimates by 27 GW and 19 GW, respectively. In order to understand the geographical distribution of the dissipation, the M_2 dissipation rate per unit area by bottom friction in regions A and B are plotted in Figs. 10 and 11. The dissipation occurs over the relatively broad area in region A reflecting large amplitude of tidal current in this

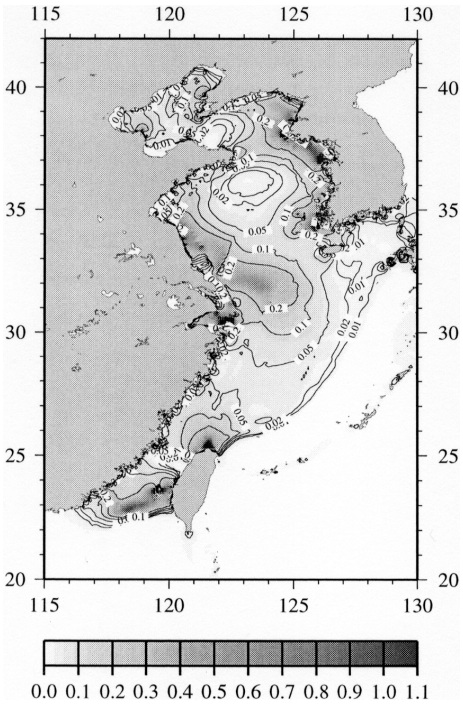

Fig. 10. M_2 tidal dissipation rate per unit area due to bottom friction in the East China Sea region. Contours are drawn at 0.01, 0.02, 0.05, 0.1 and 0.2 Wm^{-2}.

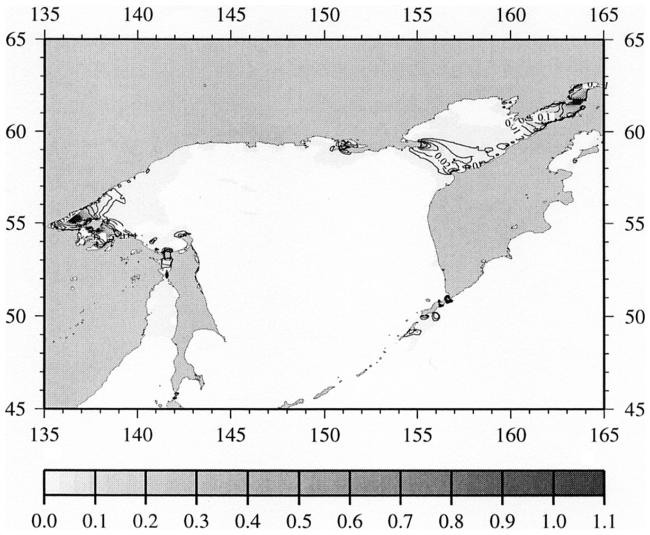

Fig. 11. Same as Fig. 10, but in the Sea of Okhotsk region.

region, but strong dissipation rate over 1 Wm^{-2} is concentrated on some small areas near coast. Although the dissipation rate in region B is generally smaller than that in region A, the characteristic of localized dissipation also applies to this region. The dissipation by eddy viscosity

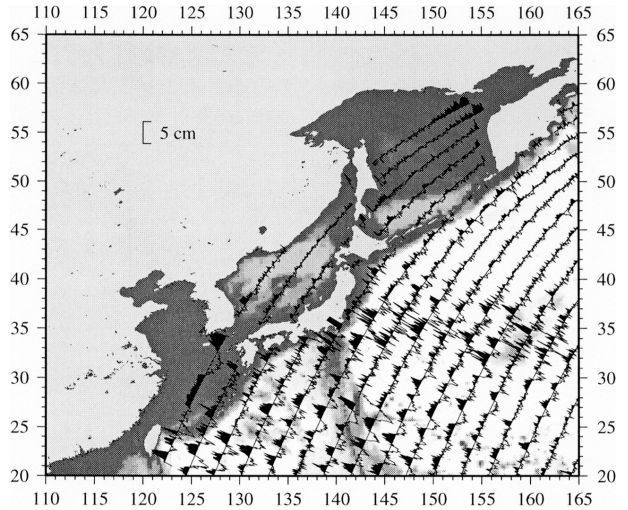

Fig. 12. High-pass filtered estimates of M_2 tidal amplitudes, plotted along 16 T/P ascending tracks. Background shading corresponds to bathymetry, with darker denoting shallower water.

is also concentrated in shallow waters, especially in island chain system, such as the Kuril Islands, the Izu-Ogasawara Islands, and Ryukyu Islands. The main sink of K_1 tidal energy is in the Sea of Okhotsk, and the mean dissipation rate over the region B is 89 GW which accounts for 81% of total dissipation within the NAO.99Jb model domain.

However, the above mentioned characteristics of localized dissipation mechanism in the shallow waters may not be representative of the real ocean, because a barotropic numerical model is unable to estimate tidal energy conversion into baroclinic tide. The internal tide signal, wavelength of that is approximately 110 km for semi-diurnal tide assuming a first mode baroclinic wave speed of 2.5 ms^{-1} (Kantha and Tierney, 1997), is also filtered out of T/P data by the along-track low-pass filtering in Section 2.

Niwa and Hibiya (1999) calculates spatial distribution of internal tidal energy flux converted from barotropic one by using a three-dimensional primitive equation numerical model, which suggests the strong generation of internal tide over spread area around the continental shelf in the East China Sea and around the Izu-Ogasawara Ridge, and some in deep seas. Their three-dimensional numerical model gives 58 GW as M_2 tidal energy flux converted into internal tide within the NAO.99Jb model domain (Niwa, personal communication), which is 21% of present barotropic estimate of M_2 tidal dissipation by NAO.99Jb. As shown by Ray and Mitchum (1997), surface manifestation of internal tides, at least its phase-locked part of the signal, can be detected by T/P altimetry.

In spite they showed the results near Hawaii, in this paper, we applied the similar analysis to the region near Japan. Plotted in Fig. 12 are high-pass filtered estimates of M_2 tidal amplitudes which are deduced from point-by-point tidal analysis for the 16 T/P ascending tracks. The altimeter data are not subjected to along-track low-pass filtering before this tidal analysis. The tidal estimates are highly contaminated by the Kuroshio near latitude of 35°N. In the region of latitude between 20°N and 30°N, however, there are clear oscillations with amplitudes of 3–4 cm and wavelength of order 150 km. These oscillations imply that internal tides are generated by the bottom topography, mainly at the Izu-Ogasawara Ridge and the continental shelf along off the Ryukyu Islands, propagating to the deep ocean. Therefor, we will investigate the subject of the energy budget of the tidal dissipation in detail through more careful analysis and discussion in order to fill the gap between the barotropic estimate and the observational evidence.

7. Summary

We have developed new global ocean tide model and loading tide model (NAO.99b model) for 16 major short-period constituents which are developed by assimilating about five years of T/P altimeter data into numerical hydrodynamical model. We also developed a regional high-resolution ocean tide model around Japan (NAO.99Jb model) which assimilates coastal tide gauge data as well as T/P data. The new models have improved the accuracy of ocean tide estimation especially in shallow waters compared with the other two existing tide models, CSR4.0 model and GOT99.2b model. This has been achieved by the following methodologies applied to the current study; (1) estimation of altimetric tides in small bins, (2) accurate tidal analysis by response method in which fine structure of admittance due to FCN resonance and radiational anomaly is taken into account, (3) precise estimation of ocean-induced self-attraction/loading effects, and (4) assimilating coastal tide gauge data into NAO.99Jb.

The accuracy of the new ocean tide models has been examined using tide gauge data and collinear residual reduction test. NAO.99b shows a comparable agreement with 98 open-ocean tide gauge data as well as CSR4.0 and GOT99.2b. The comparison with 58 shallow water tide gauges, on the other hand, supports the better accuracy of NAO.99b model in shallow seas. The local comparison with 80 coastal tide gauge data around Japan shows further improvement by NAO.99Jb. It has been also shown that NAO.99b model gives smaller collinear residuals in shallow waters than CSR4.0 and GOT99.2b.

A preliminary result has been introduced as to barotropic ocean tidal energy dissipation around Japan. The main sinks of M_2 tidal energy are the Yellow Sea—the East China Sea region and the Sea of Okhotsk region within which ocean tidal energy is dissipated at the mean rate of 155 GW and 54 GW, respectively. The K_1 tidal energy is mainly dissipated in the Sea of Okhotsk at the mean rate of 89 GW. The geographical plots of tidal dissipation suggest that the dissipation is a highly localized phenomenon in shallow seas. However T/P detects broadly distributed surface manifestation of internal tide even in deep ocean. More complete description of tidal energy budget, which includes contribution from radial loading tide, internal tide, the energy converted into shallow-water constituents, will be continued into our future work.

Acknowledgements

We are indebted to Dr. T. Yanagi for providing harmonic constants from coastal tide gauges around Korea. We are grateful to Dr. Y. Niwa for invaluable discussions on internal tidal dissipation. We are also grateful to two anonymous reviewers for their critical reading and useful comments. We are thankful to NASA JPL for preparing the TOPEX/POSEIDON altimeter data. One of the authors, Koji Matsumoto, is a research fellow of the Japan Society for the Promotion of Science.

References

Andersen, O. B., P. L. Woodworth and R. A. Flather (1995): Intercomparison of recent ocean tide models. *J. Geophys. Res*., **100**(C12), 25261–25282.

Benada, R. (1997): Merged GDR (TOPEX/POSEIDON) Generation B user's handbook. Rep. JPL D-11007, Jet Propul. Lab., Pasadena, CA.

Cartwright, D. E. and R. D. Ray (1991): Energetics of global ocean tides from Geosat altimetry. *J. Geophys. Res*., **96**(C9), 16897–16921.

Cartwright, D. E. and R. D. Ray (1994): On the radiational anomaly in the global ocean tide with reference to satellite altimetry. *Oceanologica Acta*, **17**, 453–459.

Christodoulidis, D. C., D. E. Smith, R. G. Williamson and S. M. Klosko (1988): Observed tidal braking in the Earth/Moon/Sun system. *J. Geophys. Res*., **93**, 6216–6236.

Desai, S. D. and J. Wahr (1995): Empirical ocean tide models estimated from TOPEX/POSEIDON altimetry. *J. Geophys. Res*., **100**(C12), 25205–25228.

Dickey, J. O., P. L. Binder, J. E. Faller, X. X. Newhall, R. L. Ricklefs, J. G. Ries, P. J. Shelus, C. Veillet, A. L. Whipple, J. R. Wiant, J. G. Williams and C. F. Yoder (1994): Lunar laser ranging: A continuing legacy of the Apollo program. *Science*, **265**, 482–490.

Eanes, R. J. and S. V. Bettadpur (1994): Ocean tides from two years of TOPEX/POSEIDON altimetry (abstract). *EOS Trans. AGU*, **75**(44), Fall Meet. Suppl., 61.

Egbert, G. D., A. F. Bennette and M. G. G. Foreman (1994): TOPEX/POSEIDON tides estimated using a global inverse model. *J. Geophys. Res*., **99**, 24821–24852.

Groves, G. W. and R. W. Reynolds (1975): An orthogonalized convolution method of tide prediction. *J. Geophys. Res*., **80**, 4131–4138.

Han, G., R. Hendry and M. Ikeda (2000): Assimilating TOPEX/POSEIDON derived tides in a primitive equation model over the Newfoundland Shelf. *Cont. Shelf Res.*, **20**, 83–108.

Hendershott, M. C. (1972): The effects of solid Earth deformation on global ocean tides. *Geophys. J. R. Astr. Soc.*, **29**, 389–402.

Herring, T. A., C. R. Gwinn and I. I. Shapiro (1986): Geodesy by radio interferometry: Studies of the forced nutations of the Earth, 1. Data analysis. *J. Geophys. Res.*, **91**(B5), 4745–4754.

Kantha, L. H. (1995): Barotropic tides in the global oceans from a nonlinear tidal model assimilating altimetric tides 1. Model description and results. *J. Geophys. Res.*, **100**(C12), 25283–25308.

Kantha, L. H. and C. Tierney (1997): Global baroclinic tides. *Prog. Oceanogr.*, **40**, 163–178.

Lambert, A., S. D. Pagiatakis, A. P. Billyard and H. Dragert (1998): Improved ocean tide loading correction for gravity and displacement: Canada and northern United States. *J. Geophys. Res.*, **103**(B12), 30231–30244.

Le Provost, C. and F. Lyard (1997): Energetics of the M_2 barotropic ocean tides: an estimate of bottom friction dissipation from a hydrodynamic model. *Prog. Oceanogr.*, **40**, 37–52.

Le Provost, C., M. L. Genco, F. Lyard and P. Canceil (1994): Spectroscopy of the world ocean tides from a finite element hydrodynamic model. *J. Geophys. Res.*, **99**(C12), 24777–24797.

Le Provost, C., J. M. Molines, F. Lyard, M. L. Genco and F. Rabilloud (1995): A global ocean tide prediction model based on the hydrodynamic finite element solutions FES94.1 improved by assimilation of the CSR2.0 T/P solutions (abstract). Paper presented at symposium Operational Oceanography and Satellite Observation, Biarritz, France, 1995.

Matsumoto, K. (1997): Development of a new precise ocean tide model based on satellite altimeter data. Ph.D. Thesis, University of Tokyo, 122 pp.

Matsumoto, K., M. Ooe, T. Sato and J. Segawa (1995): Ocean tide model obtained from TOPEX/POSEIDON altimetry data. *J. Geophys. Res.*, **100**(C12), 25319–25330.

Morozov, E. G. (1995): Semidiurnal internal wave global field. *Deep-Sea Res.*, **42**, 135–148.

Munk, W. H. and D. E. Cartwright (1966): Tidal spectroscopy and prediction. *Philos. Trans. R. Soc. London, Ser. A*, **259**, 533–581.

Niwa, Y. and T. Hibiya (1999): Spatial distribution of internal tides in the North Pacific predicted using a three-dimensional numerical model. *EOS Trans. AGU*, **80**(49), Ocean Sciences Meet. Suppl., OS203.

Pugh, D. T. (1987): *Tides, Surges and Mean Sea-Level*. John Wiley & Sons, 472 pp.

Ray, R. D. (1998a): Ocean self-attraction and loading in numerical tidal models. *Mar. Geod.*, **21**, 181–192.

Ray, R. D. (1998b): Spectral analysis of highly aliased sea-level signals. *J. Geophys. Res.*, **103**(C11), 24991–25003.

Ray, R. D. (1999): A global ocean tide model from TOPEX/POSEIDON altimetry: GOT99.2. NASA Tech. Memo., 209478.

Ray, R. D. and G. T. Mitchum (1997): Surface manifestation of internal tides in the deep ocean: observations from altimetry and island gauges. *Prog. Oceanogr.*, **40**, 135–162.

Ray, R. D., R. J. Eanes and B. F. Chao (1996): Detection of tidal dissipation in the solid Earth by satellite tracking and altimetry. *Nature*, **381**, 595–597.

Schwiderski, E. W. (1980): Ocean tides, I, Global ocean tidal equations. *Mar. Geod.*, **3**, 161–217.

Shum, C. K., P. L. Woodworth, O. B. Andersen, G. Egbert, O. Francis, C. King, S. Klosko, C. Le Provost, X. Li, J. Molines, M. Parke, R. Ray, M. Schlax, D. Stammer, C. Tierney, P. Vincent and C. Wunsch (1997): Accuracy assessment of recent ocean tide models. *J. Geophys. Res.*, **102**(C11), 25173–25194.

Smithson, M. J. (1992): Pelagic tidal constants—3. IAPSO Publication Scientifique No. 35. Published by the International Association for the Physical Sciences of the Ocean (IAPSO) of the International Union of Geodesy and Geophysics, 191 pp.

Wahr, J. M. (1981): Body tides on an elliptical, rotating, elastic, oceanless Earth. *Geophys. J. R. Astr. Soc.*, **64**, 677–703.

Wahr, J. M. and T. Sasao (1981): A diurnal resonance in the ocean tide and in the Earth's load response due to the resonant free "core nutation". *Geophys. J. R. Astr. Soc.*, **64**, 747–765.